CrossMark

AOPS: RECENT ADVANCES TO OVERCOME BARRIERS IN THE TREATMENT OF WATER, WASTEWATER AND AIR

Magnetic iron species highly dispersed over silica: use as catalysts for removal of pollutants in water

Victor A. A. Freitas[1] · Laura A. Maia[1] · Rolando E. Belardinelli[2] · Jose D. Ardisson[3] ·
Márcio C. Pereira[4] · Luiz C. A. Oliveira[1]

Abstract Fe_2O_3-SiO_2 composites were prepared by impregnation (sample FeIMP) or doping (sample FeDOP) in the structure of porous silica. The dye removal capacity of the materials was investigated through adsorption and oxidation studies of methylene blue and rhodamine B. N_2 adsorption/desorption measurements on FeIMP and FeDOP resulted in specific areas of 27 and 235 m^2 g^{-1}, respectively. Mössbauer spectroscopy and XRD data detected hematite and maghemite as the iron phases in the samples FeIMP and FeDOP, respectively. Adsorption isotherms and kinetic studies of the dyes were better fitted in DKR model for FeDOP, where the process follows a pseudo-second order with the interparticle diffusion step being the rate-limiting step. On the other hand, FeIMP has better fit in the Langmuir model. Photocatalytic activity was observed in FeDOP under UV irradiation by the presence of reaction-hydroxylated intermediates for MB (m/z = 301) and RhB (m/z = 459). However, the photocatalytic activity was strongly influenced by the adsorption affinity between dye/catalyst. Photogenerated holes are the species responsible for the dye degradation when the adsorption is too strong, while hydroxyl radical action will be favored when the adsorption is not vigorous as detected by ESI-MS.

Keywords Photocatalysis · Iron oxide · Adsorption · DKR · Kinetic · Photogenerated species

✉ Victor A. A. Freitas
victoraugusto.freitas@gmail.com

[1] Department of Chemistry, UFMG, Av. Antônio Carlos,
6627—Pampulha, 31270-901 Belo Horizonte, Minas Gerais, Brazil

[2] Department of Physics, School of Mathematics, Physics, and Natural Sciences, UNSL, CONICET, Ejercito de Los Andes 950, San Luis, Argentina

[3] CDTN, Av. Pres. Antônio Carlos, 6.627 - Campus UFMG, 31270-901 Belo Horizonte, Minas Gerais, Brazil

[4] UFVJM, Institute of Science, Engineering, and Technology, Rua Cruzeiro, 1—Jardim São Paulo, 39803-371 Teófilo Otoni, Minas Gerais, Brazil

Introduction

The textile industry is one of the biggest producers of industrial wastewater, which usually contains a complex mixture of chemicals used in the different dyeing and finishing process steps. Those chemicals could harm the environment if not properly treated before discharge. High concentration of dyes in natural water bodies can change the light penetration index, which disturbs the entire aquatic system. Also, the increasing in public awareness related to environmental issues pushes the industries to decrease the pollutant emissions as much as possible.

Usually, synthetic dyes are, besides being derived mostly from coal tar or petroleum intermediates, also commonly recalcitrant, toxic, and non-biodegradable. It is estimated that for each 1 kg of clothing in dyeing and finishing plants, about 280 L of water is consumed (Ajmal et al. 2014). Projections from the United Nations (2015) claim that by 2050, the world's population would have grown about 32 % when compared to 2015. Accordingly, world dye production and consumption will continuously increase with the world's

Springer

population growth rate (Hasanbeigi and Price 2015; United Nations Department of Economic and Social Affairs 2015). Therefore, the existing treatment methods must be constantly improved to meet the increasingly restrictive water discharge regulations imposed by governments. An alternative is to enhance the treatment efficiency by developing new materials capable of removing those pollutants from aqueous media.

The advanced oxidation process (AOP)-based technologies demonstrate their usefulness as a tool for wastewater treatment since the process can degrade various high molecular weight, toxic, and recalcitrant organic compounds into those of low molecular weight and less toxic, increasing their biodegradability and even reaching complete mineralization. This outstanding performance of AOP is due to the in situ generation of radicals such as $^{\bullet}OH$, $^{\bullet}OOH$, and $^{\bullet -}O_2$, which are extremely reactive, non-selective, and strong oxidizing agents ($E^o = 2.8$ V vs. NHE) (Marcelino et al. 2014). The radicals are formed when a semiconductor is irradiated with a proper light wavelength that promotes the generation of free electrons (e^-) and electronic holes (h^+).

Iron oxides exhibit narrow band-gap energies (2.0–2.4 eV) depending on which crystalline phase is chosen. Materials based on iron oxides can be easily synthesized even on a large scale besides being widely found in nature, which makes them a feasible option as photocatalysts (Wu et al. 2015). They have been successfully used in industrial effluent treatment methods, especially in color removal from wastewater from industries using organic dyes at some stage of their processes.

Among the most commonly used iron oxides in environmental remediation, the Fe_2O_3 phases (hematite, α-Fe_2O_3, and maghemite, γ-Fe_2O_3) are excellent candidates due to their chemical and physical properties. It crystallizes more commonly as (i) hematite (α-Fe_2O_3), isostructural with corundum with all metal sites octahedrally coordinated and occupied by Fe^{3+}. These oxides can reach a specific area of 5–100 m^2 g^{-1}, depending on the synthetic route (Schwertmann and Cornell 1991), and (ii) maghemite (γ-Fe_2O_3) under the Fd3m cubic system, having magnetic activity and, depending on the synthesis route, can reach a specific area from 8 to 130 m^2 g^{-1} (Schwertmann and Cornell 2003). All the Fe atoms are in the trivalent state, and cationic vacancies exist in their structure.

However, iron oxides have two major drawbacks to being used as photocatalysts: (i) high electron-hole recombination rate and (ii) short h^+ diffusion length. Both of those drawbacks can be overcome by finely dispersing the iron oxide particles in a surface matrix such as silica, carbon, clay minerals, zeolites, etc. Also, the relation of how the adsorption strength affects the generation of •OH and h^+ has not been fully discussed elsewhere.

Therefore, the main goal of this work was to synthesize a material based on iron oxide with high specific area and evaluate its adsorption capacity against organic dyes and photocatalytic activity as well as understand how the adsorption affects the photocatalytic mechanism.

Materials and methods

Synthesis of the silica support

A mesoporous silica support was obtained using tetraethyl orthosilicate (TEOS) as a silicon source and cetyltrimethylammonium bromide (CTAB) as surfactant in alkaline media. First, CTAB (16.3 g, Vetec) was solubilized in 200 mL of deionized water and mixed with 100 mL of NaOH (1 mol L^{-1}, Aldrich). Then, 37 mL of TEOS was slowly dripped under magnetic stirring at room temperature for 24 h. The solid obtained was centrifuged and washed with deionized water until pH 7 and dried at 70 °C for 12 h. This procedure leads to the production of a mesoporous silica, which was used as a support to produce iron oxides with high specific areas.

Synthesis of iron oxides

In order to increase the surface area of the iron oxide, two different approaches were conducted: (i) 5 g of the silica support, synthesized as described above, was mixed with 50 mL of an $Fe(NO_3)_3$·$9H_2O$ (1.25 mol, Aldrich) solution and magnetically stirred for 2 h at room temperature (molar composition Si^{4+}/Fe^{3+} 1.00:3.67). The mixture was filtered and dried at 80 °C for 12 h and then calcined at 600 °C for 5 h. The material was then treated with NaOH according to the proposal by Bjørgen et al. (2008) and consists of two washings with a 0.2 mol L^{-1} NaOH solution at 65 °C for 4 h, followed by washing with deionized water at 80 °C for 1 h. The final product was centrifuged and dried at 80 °C to produce the sample Fe-DOP. (ii) The second approach uses the silica support after a calcination step at 550 °C for 5 h. The impregnated catalyst (Fe-IMP) was prepared by mixing 25 mL of iron solution with 5 g of the calcined silica precursor for 30 min at 60 °C followed by slow drying at 80 °C (molar composition Si^{4+}/Fe^{3+} 1.00:4.41). The mixture was dried at 80 °C for 12 h, calcined at 600 °C for 5 h, and submitted to an alkaline treatment as described above.

Characterization of the catalysts

The crystalline phases were determined by X-ray diffraction (XRD) using CuKα radiation from a 20 to 70°/2θ range. The patterns were compared with cards from Mincryst database. Mössbauer spectra were collected at 298 and 77 K in 1024 channels using a ^{57}Co/Rh source with Doppler velocities in the range of ±10 mm s^{-1}. α-Fe foil was used as a standard. Diffuse reflectance spectra were collected in a UV-2600

Shimadzu spectrophotometer, with diffuse reflectance accessory in the 180–800-nm range and 0.5-nm resolution. The temperature-programmed reduction (TPR) profiles were obtained in H_2 flux in a ChemBET 3000 equipment from Quantachrome equipped with a TCD detector at a heating rate of 10 °C min^{-1} and under H_2 flux at 80 mL min^{-1}. Textural properties were determined via N_2 adsorption at −196 °C in an Autosorb-1 Quantachrome system. The samples were previously degassed at 110 °C for 10 h, and the specific area was calculated using the BET model. Transmission electron microscopy (TEM) images were taken with a JEOL transmission electron microscope model JEM 2000EXII. Energy-dispersive X-ray spectroscopy (EDS) data were collected using an EDS/INCA 350 equipment.

Adsorption studies

The kinetic curves and the adsorption isotherms were conducted at 25 °C and pH = 5.5 using 10 mg of adsorbent in 10 mL of methylene blue solution. The adsorption isotherm was constructed with dye concentrations of 20, 50, 100, 200, and 500 mg L^{-1} during 4 h of contact. The removal percentage was measured using UV-Vis spectrophotometer (Shimadzu) and quantified by Eq. (1).

$$Removal\ (\%) = \frac{(C_0 - C_f)}{C_0} \times 100 \tag{1}$$

The adsorption isotherm data were fitted using three different models.

Langmuir isotherm

The Langmuir empirical model assumes active site energy homogeneity, where adsorption is done in a monolayer, and there is no interaction or steric hindrance between adsorbate molecules, even in adjacent sites. Each adsorbate molecule has equivalent enthalpy and adsorption energy, there being no transmigration occurring among active sites.

$$q_{eq} = \frac{QobCe}{1 + bCe} \tag{2}$$

By linearizing, it becomes

$$\frac{Ce}{q_{eq}} = \frac{1}{bQo} + \frac{Ce}{Qo} \tag{3}$$

where q_{eq} is the amount of adsorbate adsorbed at equilibrium, Q_o is the maximum amount of adsorption, Ce is the concentration of adsorbate at equilibrium, and b is the Langmuir constant.

Freundlich isotherm

This model describes an ideal and non-reversible adsorption process. The surface adsorption presents a non-uniform active site energy distribution (heat and activity). However, the deviation from Henry's law, especially at low adsorbate concentrations, makes this model strongly criticized.

$$q_{eq} = KfCe^{1/n} \tag{4}$$

In the linear form, it becomes

$$\log q_{eq} = \log Kf + \frac{1}{n}\log Ce \tag{5}$$

where Q_e and C_e have the same meaning as described in the Langmuir model; K_f and n are Freundlich constants.

Dubinin-Kaganer-Radushkevich isotherm

The Dubinin-Kaganer-Radushkevich (DKR) isotherm is also a hybrid between the Langmuir and Freundlich, assuming an energetically inhomogeneous surface or one of constant adsorption potential. It is thus possible to calculate the apparent adsorption energy and take into account the porosity of the adsorbent (Cortes and Araya 1986; Foo and Hameed 2010).

$$q_{eq} = \frac{RT}{b_t}\ln A_t + \frac{RT}{b_t}\ln Ce \tag{6}$$

The linear form is

$$\ln q_{eq} = \ln Qo - \beta\varepsilon^2 \tag{7}$$

where

$$\varepsilon = RT\ln\left(1 + \frac{1}{Ce}\right) \tag{8}$$

Catalytic tests

Degradation tests of methylene blue dye at a concentration of 100 ppm were conducted in a fixed bed reactor with a 100-mL capacity at 20 °C using 60 mg of catalyst and 80 mL of the dye solution at pH 6 (25 °C). The reactions were performed under UV (Hg lamp) and visible light irradiation (W lamp). The reaction progress was monitored by UV-Vis spectroscopy at 665 nm.

To identify the intermediate chemical species of the methylene blue oxidation reaction, an LCQ Fleet ion trap mass spectrometer (Thermo Scientific) was used in positive ion mode. The reaction samples were analyzed by introducing aliquots into an electrospray ionization mass spectrometer (ESI-MS) source with a syringe pump at a flow rate of
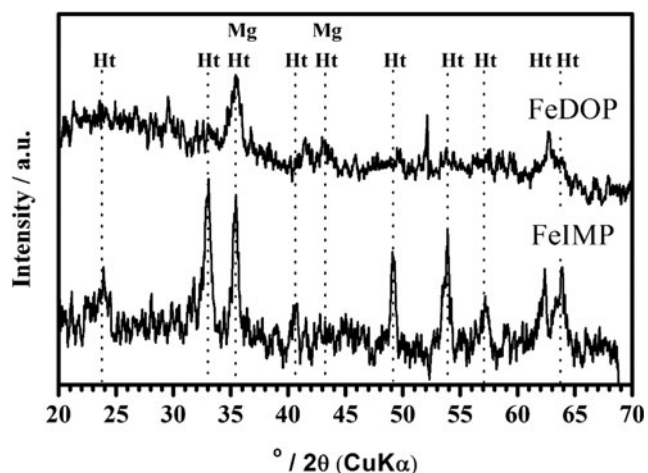
Fig. 1 X-ray diffraction patterns of the FeDOP and FeIMP samples

15 L min^{-1}. Spectra were obtained as averages of five scans of 0.2 s each. Typical ESI conditions used were as follows: heated capillary temperature of 275 °C, sheath gas (N_2) at a flow rate of 15 units (ca. 4 L min^{-1}), spray voltage of 2 kV, capillary voltage of 25 V, and tube lens offset voltage of 25 V.

Results and discussion

Characterization of the catalysts

The XRD profile of the FeIMP sample (Fig. 1) showed characteristic reflections of hematite (α-Fe_2O_3) crystalline phase, while the XRD pattern of the FeDOP sample (Fig. 1) showed

reflections attributed to maghemite crystalline phase (γ-Fe_2O_3). Using the *Unitcell* software, it was possible to determine the parameter a = 0.835 nm, confirming the presence of the maghemite crystalline phase in the FeDOP sample (Schwertmann and Cornell 2003). However, both XRD patterns presented low signal/noise ratios, suggesting that the materials have low crystallinity, which might indicate a high dispersion on the mesoporous silica surface.

The geometry and oxidation state of iron can be determined by Mössbauer spectroscopy. The Mössbauer spectrum of the FeDOP sample at 298 K shows a broad sextet and a doublet, due to the superparamagnetic relaxation phenomenon of iron oxides (Fig. 2). This spectral profile suggests high iron oxide crystal dispersion. The Mössbauer spectra of sample FeIMP showed a well-defined sextet at 298 K (Fig. 2) with an octahedral Fe^{3+} site, typical of hematite.

Low-temperature Mössbauer spectroscopy (20 K) allows the nuclear coupling to occur more efficiently, which is confirmed by the appearance of a sextet in the FeDOP sample (Fig. 2). The hyperfine parameters show the presence of Fe^{3+} in octahedral sites, typical of the maghemite phase (Table 1) as diagnosed by XRD. It is also possible to verify the presence of hematite by the discrete sextet with B_{hf} = 52 T. The hyperfine parameters of the central doublet indicate the presence of Fe^{3+} superparamagnetic species that may replace Si^{4+} in the silica, constituting a [-Si-O-Fe-O-Si-] phase. All the fitted hyperfine parameters are shown in Table 1.

An interesting technique to analyze the reactivity of the iron species present in the samples is temperature-programmed reduction (TPR-H_2). The TPR-H_2 profile of the FeDOP sample (Fig. 3) showed three events that inform about
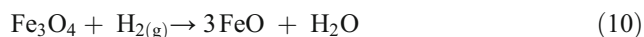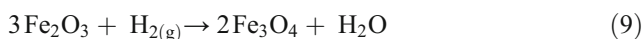
Fig. 2 Mössbauer spectra, at 298 K, of the samples FeDOP (**a**) and FeIMP (**b**) and at 20 K of FeDOP (**c**) and FeIMP (**d**)
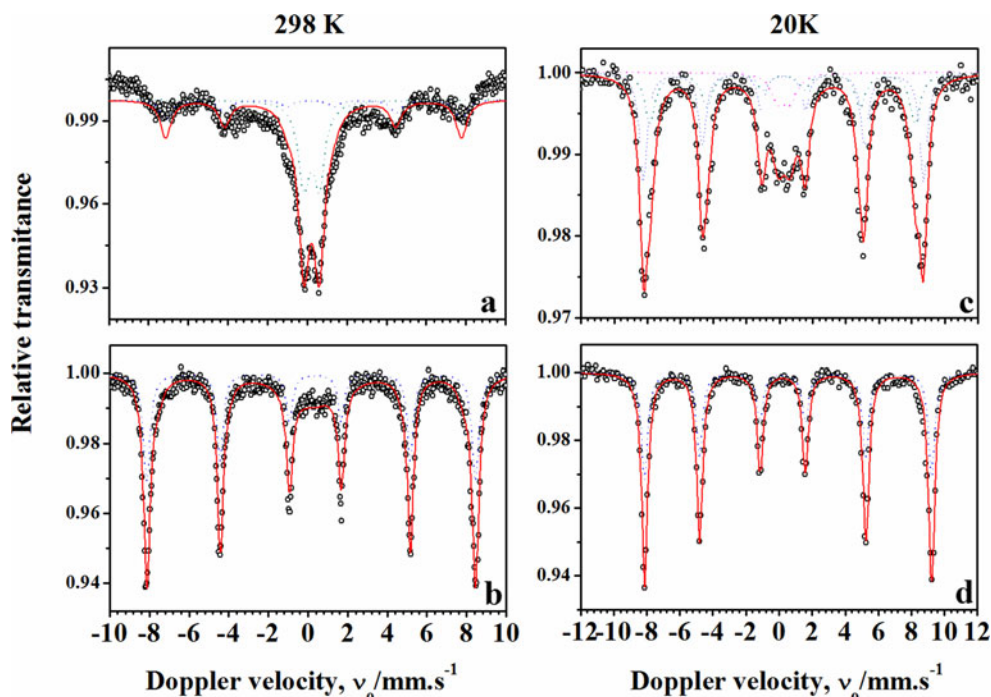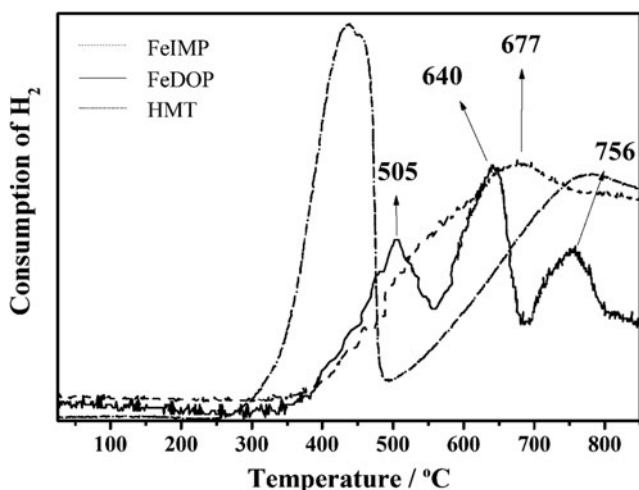
Table 1 Hyperfine parameters of the samples FeDOP and FeIMP relative to α-Fe obtained via Mössbauer spectroscopy at 298 and 20 K

Temperature/K	Sample	δ/ mm s^{-1}	Δ or 2ε/	B_{hf}/T	AR/%	Fe site	Crystalline phase
298	FeDOP	0.35	0.16	46.2	31	$^{VI}Fe^{3+}$	?
		0.34	0.77		69	$^{VI}Fe^{3+}$	?
	FeIMP	0.35	0.02	51.0		$^{VI}Fe^{3+}$	α-Fe$_2$O$_3$
20	FeDOP	0.48	0.16	53.0	9	$^{VI}Fe^{3+}$	α-Fe$_2$O$_3$
		0.43	−0.04	49.9	41	$^{IV}Fe^{3+}$	γ-Fe$_2$O$_3$
		0.45	0.00	52.4	37	$^{VI}Fe^{3+}$	γ-Fe$_2$O$_3$
		0.48	0.74	–	13	$^{IV}Fe^{3+}$	Fe-Si
	FeIMP	0.47	0.36	53.9	67	$^{VI}Fe^{3+}$	α-Fe$_2$O$_3$
		0.46	0.23	52.1	25	$^{VI}Fe^{3+}$	α-Fe$_2$O$_3$

the reduction of the iron phases: maghemite or hematite → magnetite → Wüstite → metallic iron (Schwertmann and Cornell 2003). The temperature range for the reduction of iron oxides to metallic iron in the FeDOP material is higher compared with that of FeIMP, reinforcing the existence of species [-Si-O-Fe-O-Si-] that shift the reduction temperatures to higher values. The FeIMP material resulted in a typical hematite reduction profile with maxima at 640 and 677 °C. The reduction steps are described in Eqs. 9, 10, and 11. Interaction between the silica support and Fe atoms could be observed by the temperature reduction shift to higher values compared to pure hematite (HMT)

$$3\,Fe_2O_3 + H_{2(g)} \rightarrow 2\,Fe_3O_4 + H_2O \tag{9}$$

$$Fe_3O_4 + H_{2(g)} \rightarrow 3\,FeO + H_2O \tag{10}$$

$$FeO + H_{2(g)} \rightarrow Fe^0 + H_2O \tag{11}$$

$N_{2(g)}$ adsorption-desorption isotherm of the FeDOP sample (Fig. 4) shows a type IV hysteresis typical from mesoporous materials with strong adsorbent-adsorbate interaction and interparticle pore type. The specific area estimated from BJH method is 235 m^2 g^{-1} with 57 nm pore diameter. On the contrary, the FeIMP sample did not develop a high specific area, 27 m^2 g^{-1}, which is in the same value range of regular hematite. Considering the FeIMP isotherm profile, it can be said that either the sintering process or structural collapsing of the silicate might have occurred during the calcination step.

Finally, the morphology of the materials was determined by TEM. The FeDOP micrographs are shown in Fig. 5. TEM images obtained using atomic mass as contrasts show, for the FeDOP sample, irregular agglomerates with average sizes of 150 nm and intraparticle pores as suggested by adsorption/desorption of the $N_{2(g)}$ isotherm (Fig. 5b). Darker areas were observed when the resolution was increased (Fig. 5c) where the EDS probe showed to be more iron-rich compared to the lighter areas that are rich in silicon. The iron-rich areas (Fig. 5c) show spacing between atomic planes, with typical values of maghemite oriented in planes (311), $d = 0.2532$ nm. This crystallographic plane was detected in XRD (35°/2θ).

The FeIMP sample shows irregular agglomerates with an average size of 200 nm (Fig. 6). Lattice fringes with

Fig. 3 TPR-H$_2$ reduction profile of FeDOP, FeIMP, and hematite (HMT)
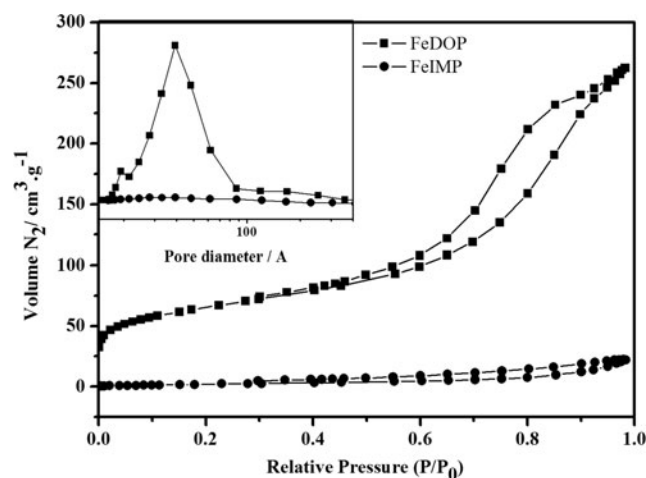
Fig. 4 $N_{2(g)}$ adsorption-desorption isotherms of FeDOP and FeIMP and, in detail, the pore size distribution

Fig. 5 TEM images and elemental analysis by EDS of FeDOP
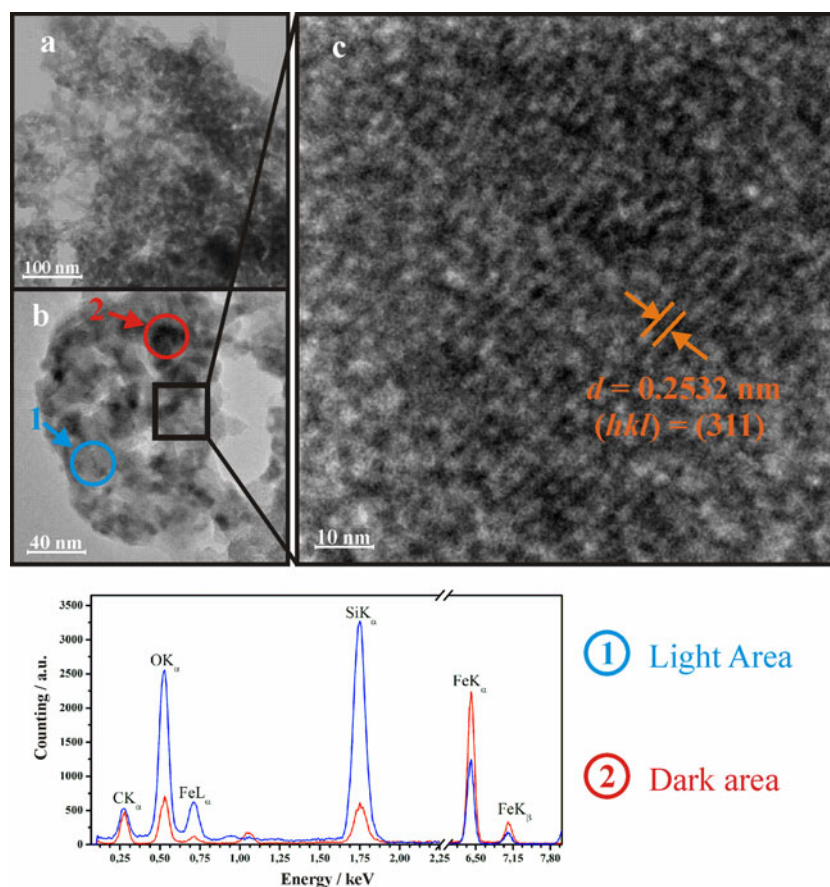
spacing $d = 0.3743$ nm were observed in the darker areas, very close to that found in the plane (012) of hematite (Fig. 6c). Only in peripheral regions of the agglomerate were those lattice fringes clearly observed (region 1, Fig. 6a), indicating that the central region is thicker than the peripheral region. The analysis by EDS probe showed that the iron concentration is higher in the central region of the agglomerate while peripheral regions are rich in silicon (Fig. 6). Bigger, thicker, randomly oriented hematite crystals were observed in the central region overlapping each other as shown by the electron diffraction ring pattern (Fig. 6a, region 2). This suggests that a dessilication step allowed hematite crystals to grow further.

For the photocatalysis study, one of the most important parameters is how much energy is necessary to promote an electron from the valence band to the conduction band (band gap). The electronic transition should promote the generation of an electron-hole pair that decomposes H_2O into highly reactive $^\bullet OH$ radical (Litter 1999; Ohtani 2010). The band gap magnitude of the materials was determined via diffuse reflectance spectroscopy in the UV-Vis region using the Kubelka-Munk formalism (Ohtani 2010). The $[F(R)hv]^n$ versus hv graph or Kubelka-Munk function versus hv provides an

excellent approximation of the band gap magnitude by graphic extrapolion (Fig. 7). The indirect band gap values determined for both materials are 2.07 and 2.04 eV for FeIMP and FeDOP, respectively.

Adsorption isotherms

Initially, the adsorption phenomena were studied to better understand the dye removal mechanisms involved in the process. The FeDOP and FeIMP materials showed a large difference in the adsorption curve profile (Fig. 8), with an adsorption capacity of approximately 80 and 15 mg g^{-1}, respectively. These results show that the accessibility of the adsorption sites is greatly influenced by the specific area of each material as expected.

Table 2 presents all data calculated from the experimental fitting data to the linear curves on different models considered. Freundlich, Langmuir, and DKR were evaluated, and it was found that the Freundlich model proved to be the least suitable to describe the adsorption isotherm in both materials. The Langmuir model along with DKR, which blends Langmuir and Freundlich models, obtained a good linear correlation with $R^2 > 0.99$. However, we must

**Fig. 6** TEM images of FeIMP with elemental analysis by EDS and electron diffraction

① Edge
② Center
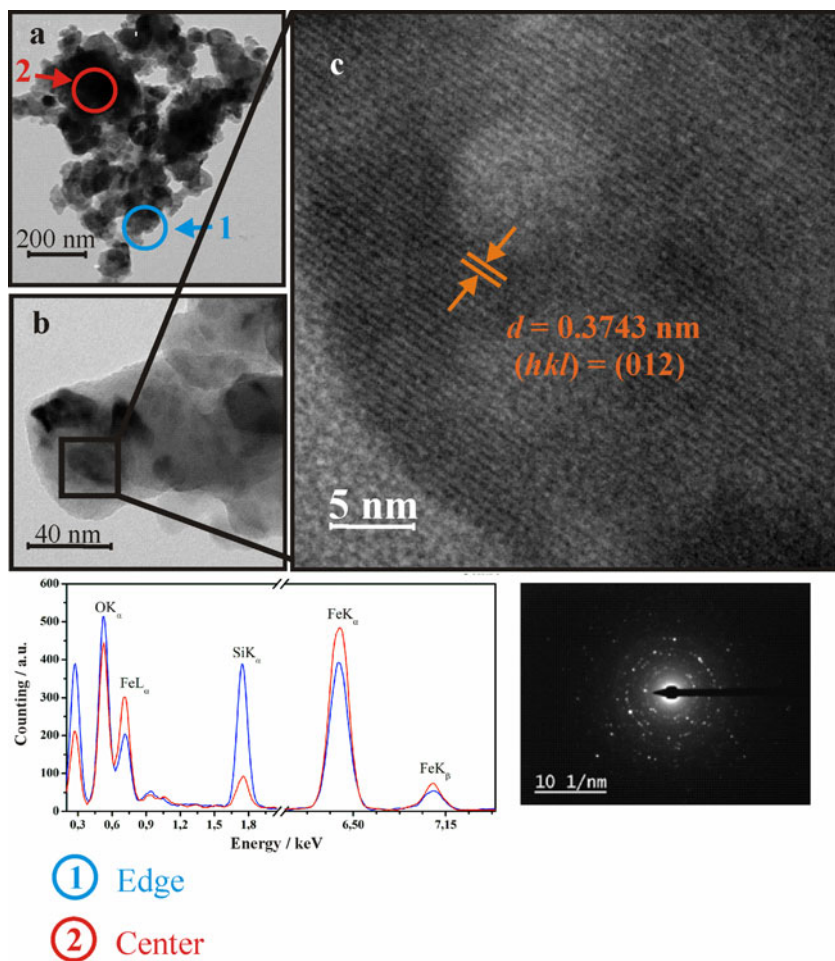
take into account that the linear correlation (R^2) parameter alone is not sufficient to determine whether a given model is satisfactory. Thus, other error estimates were calculated: χ^2 and SSE (Table 2) that allow to adjust the experimental

data to non-linearized models (Fig. 9). The DKR model, which assumes a non-constant sorption potential, resulted to be the best model to describe the adsorption process on
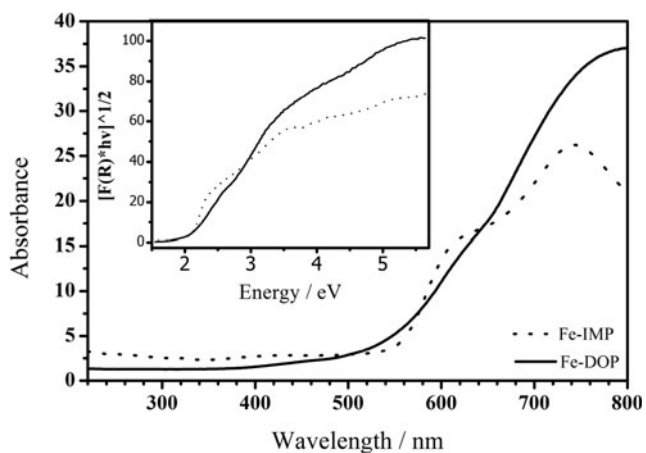
Fig. 7 UV-DRS of FeDOP and FeIMP. Detail: Kubelka-Munk formalism
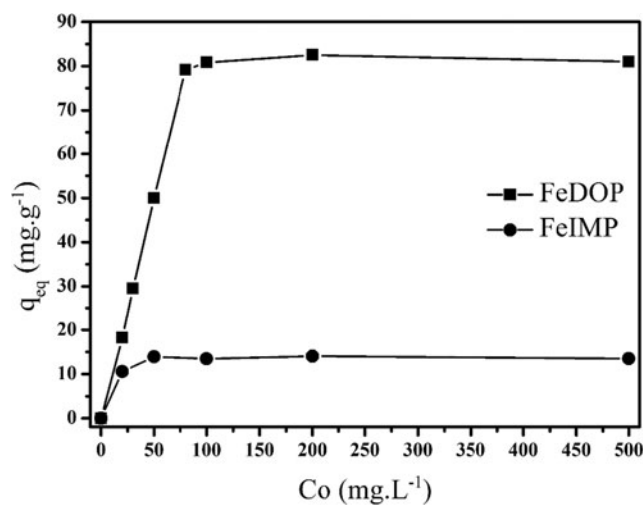
Fig. 8 Methylene blue adsorption isotherms at 100 mg L^{-1}, 80 mL of solution, and 60 mg of the FeDOP and FeIMP material

Table 2 Adsorption parameters estimated by different models for the FeDOP and FeIMP materials with their respective error analysis

| Adsorption model	Adsorption parameters		Errors and relative correlations		
Langmuir	Qeq (mg g^{-1})	b (dm^3 g^{-1})	R^2	χ^2	SSE
FeDOP	81.30	0.55	0.998	1.64	72.59
FeIMP	13.51	0.89	0.999	4.22	56.15
Freundlich	1/n	Kf	R^2	χ^2	SSE
FeDOP	0.16	38.17	0.524	18.66	1078.66
FeIMP	0.05	10.13	0.543	4.09	53.41
DKR	Qeq (mg g^{-1})	E (kJ mol^{-1})	R^2	χ^2	SSE
FeDOP	84.97	1.29	0.950	0.28	22.96
FeIMP	13.90	0.35	0.974	4.42	61.53

FeDOP, while FeIMP already had a satisfactory result with the classic Langmuir model.

Adsorption kinetic and photocatalytic mechanism

The adsorption kinetic study allows to explain the solute sorption rate. It is evident that the rate controls the adsorbate adsorption residence time at the solid-liquid interface. The methylene blue adsorption kinetics over the FeDOP and FeIMP materials was investigated using pseudo-first-order (Lagergren) and pseudo-second-order (Elovich) models and intraparticle diffusion in their respective linear forms (Fig. 10) (Al-anber and Al-anber 2008; Alihosseini et al. 2010).

The FeDOP and FeIMP materials resulted in a better fit when modeled with the standard pseudo-second-order model (Eq. 12), where each adsorbate molecule occupies two adsorption sites of the adsorbent (Gong et al. 2009).

$$\frac{dq_t}{dt} = K_2(Q_0 - Q_t)^2 \tag{12}$$
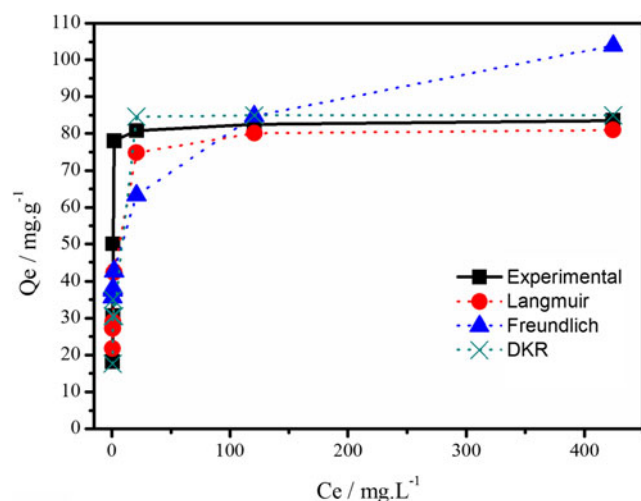
Fig. 9 Non-linear adjustment of different adsorption isotherm models for the 10-mg FeDOP with 10 mL methylene blue at 100 ppm at 25 °C and pH = 5.5

where Q_0 is the initial amount of solute in solution, Qt is the amount of solute adsorbed on an adsorbent mass m at time t, and K_2 is the adsorption kinetic constant. Integrating Eq. (12) in the boundary conditions $t = 0$ at $t = t$ and $Qt = 0$ at $Qt = Qt$ in the limits of the experiment and then rearranging it, we obtain the linear form (13), making it possible to build a graph of $1/Q_t$ versus time:

$$\frac{t}{Q_t} = \frac{1}{K_2 Q_0^2} + \frac{1}{Q_0} t \tag{13}$$

where the term $K_2 Q_0^2 = h = $ mg g^{-1} min^{-1} is the initial adsorption rate.

The interparticle diffusion model was described by Weber and Morris (1963) and Srivastava et al. (1989) in linear form:

$$qt = K_p t^{0,5} + C \tag{14}$$

where K_p is the rate constant interparticle diffusion expressed in mg g^{-1} min$^{0.5}$ and C is the intercept of the curve.

The interparticle diffusion process should also be considered due to the good fit of the experimental data (Table 3). In particular, in the case of the FeDOP material, two distinct linear regions can be determined in the Qt versus $t^{0.5}$ graph (Fig. 11). According to Wu et al. (2009) and Sun and Yang (2003), the multilinearity observed indicates that two or more steps in the adsorption process are occurring. The first is assigned to the quick adsorption step, whereas the second stage is the gradual adsorption, where the interparticle diffusion limits the kinetic rate. Thus, the adsorption process in the FeDOP material, even following the pseudo-second-order model, has its sorption rate controlled by interparticle diffusion (Sun and Yang 2003; Wu et al. 2009).

The FeIMP material does not present interparticle diffusion ($R^2 = 0.067$) and, therefore, follows a rate controlled only by the pseudo-second-order model, which makes this material reach the surface saturation point faster when compared to FeDOP. The effect of specific area and porosity of the material can be clearly observed upon adjustment of the kinetic data; the material with the larger area and porosity has a slower

Fig. 10 a Adsorption kinetics of 10 mL of methylene blue dye at 100 mg L^{-1} over 10 mg of FeDOP and of FeIMP at 25 °C in natural pH and **b** pseudo-second-order linearized kinetic adjustments for FeDOP and FeIMP
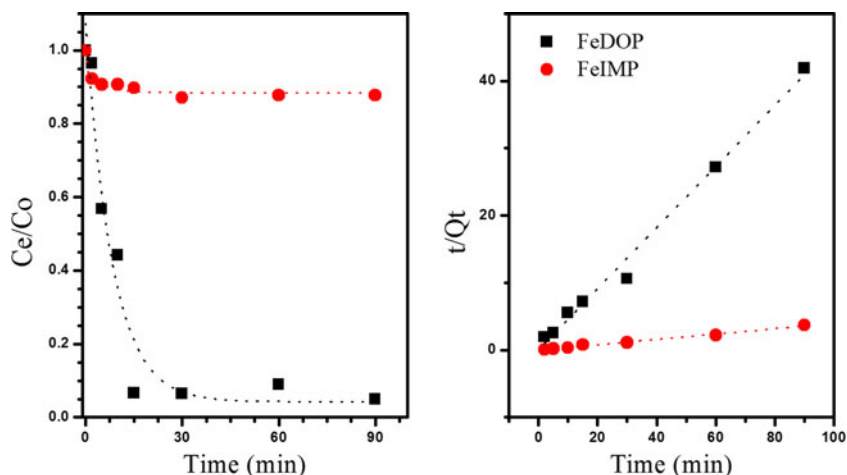
kinetics compared to materials with smaller area and low specific area.

Methylene blue removal: adsorption versus photocatalytic degradation

Under the experimental conditions used, the FeDOP material removed a total of 73 % (Fig. 12). The FeIMP material, due to the low specific surface area, showed a low dye removal capacity via the photocatalytic process. To identify the dispersion effect of the iron oxide phase over silica support, the same photocatalysis test was conducted with standards maghemite (MG) and hematite (HM). Under the same experimental conditions, the photocatalytic activity of the standard materials were practically zero (Fig. 12). Moreover, during the first 60 min of equilibrium time, the saturation point is reached in both FeDOP and silica support with no significant change during UV irradiation on the latter. The photolysis of methylene blue is negligible during the whole irradiation time, which represents less than 5 % of total dye removal after 150 min (Fig. 12).

The pseudo-second-order model gave the best fit describing the degradation kinetic of MB on FeDOP, which indicates that the degradation rate does not depend upon the initial dye concentration but upon active site availability (Fig. 13).

Table 3 Kinetic parameters of FeDOP and FeIMP materials estimated via pseudo-second-order and interparticle diffusion models

| Material	Kinetic model			
	Pseudo-second order		Interparticle diffusion	
	R^2	K_2 (g mg^{-1} min^{-1})	R^2	K_p (mg/g $min^{1/2}$)
FeDOP	0.9910	33.69	0.952/0.971	−14.80/−0.14
FeIMP	0.9911	0.18	0.067	–

Although the most commonly accepted photocatalytic degradation mechanisms are through the photogenerated $^{\bullet}OH$ radicals, we do have to consider the contribution made by other species like photogenerated h_{vb}^+. For that reason, new experiments were conducted under the presence of the scavengers DMSO and EDTA for trapping $^{\bullet}OH$ and h_{vb}^+, respectively.

The photocatalytic degradation rate of MB decreased by 8.46 and 11.67 % in the presence of DMSO and EDTA, respectively (Fig. 13). Thus, it seems that photogenerated h_{vb}^+ plays an important role in the dye degradation, and its contribution cannot be neglected. This result indicates that the most probable mechanism of MB degradation is first by h_{vb}^+ species followed by $^{\bullet}OH$ radicals, which agrees with the strong adsorptive capacity of FeDOP. If the semiconductor surface is fully covered by adsorbate molecules, then water molecules cannot reach its surface and the $^{\bullet}OH$ generation will be compromised (Eqs. 15 and 20) (Silva et al. 2009; Ohtani 2010).

Experiments using another dye (Rhodamine B) as molecular probe were conducted to confirm this hypothesis. The
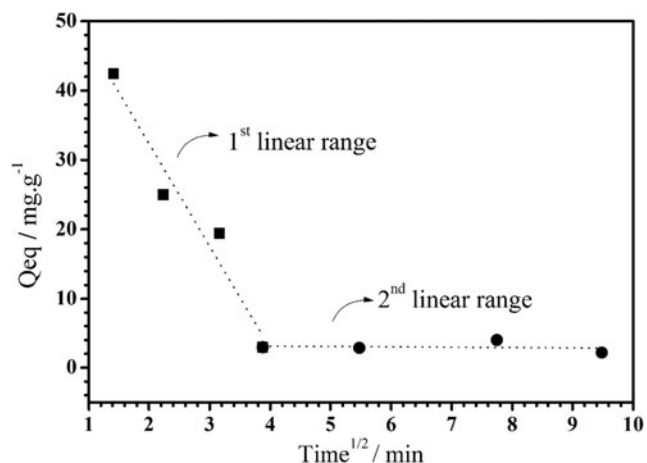
Fig. 11 Multilinear kinetic model of the FeDOP material interparticle diffusion
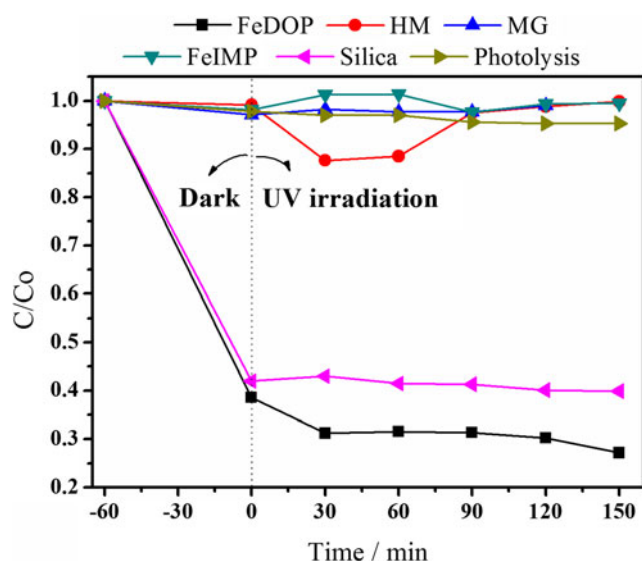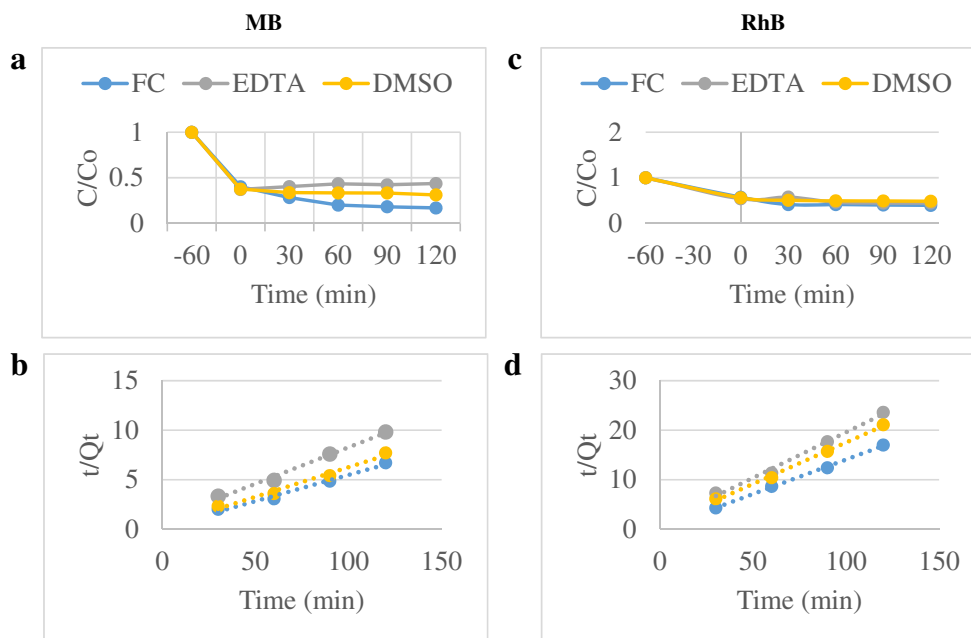
Fig. 12 Kinetics of photocatalytic degradation of MB for the FeDOP and FeIMP samples

choice of changing the substrate rather than other variables such as pH and the temperature is based on the intention to not disturb the photocatalyst surface. The experimental conditions were the same as those used before with MB (catalyst weight 60 mg, solution volume 80 mL, dye concentration 20 mg L^{-1}, and room temperature).

Adsorption study of RhB exhibits the same trend of good fitting for Langmuir's model observed for MB dye (Table 4). However, $Q_{max} = 15.45$ mg g^{-1} shows a lower affinity between adsorbate/adsorbent measure by the parameter R_L in the Langmuir adsorption model. R_L values >1 means that the adsorption process is unfavorable, $R_L = 1$ is linear, favorable if $0 < R_L < 1$, and irreversible if $R_L = 0$. According to
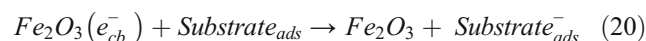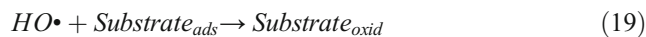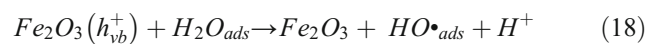
parameter R_L, the FeDOP material has more affinity for MB ($R_L = 0.03$) molecules than RhB ($R_L = 0.10$).

As with MB, the kinetic adsorption model for RhB with the best fit was the pseudo-second-order (Fig. 13, Table 1). The photocatalysis reaction without scavenger presence (FC) converged to a kinetic pseudo-second-order constant (K_2) of 9.73×10^{-7} and 0.1248 for MB and RhB, respectively. The decrease in the K_2 value indicates the effective role of the species in the photocatalytic process. With MB as a substrate, the K_2 value was strongly affected by the presence of EDTA while RhB was affected at the same proportion by the presence of both EDTA and DMSO.

This result clearly reflects the influence of adsorption capacity of the photocatalytic process. Photogenerated h_{vb}^{+} are the most active species when a strong adsorption takes place. Otherwise, radical species such as $^{\bullet}OH$ will play the major role in the photocatalytic degradation if the adsorption process is not too vigorous.

$$Fe_2O_3 + h\nu \rightarrow Fe_2O_3\left(e_{cb}^{-}, \ h_{vb}^{+}\right) \tag{15}$$

$$Fe_2O_3\left(h_{vb}^{+}\right) + Substrate_{ads} \rightarrow Fe_2O_3 + Substrate_{ads}^{+} \tag{16}$$

$$Fe_2O_3\left(h_{vb}^{+}\right) + HO_{ads}^{-} \rightarrow Fe_2O_3 + HO\bullet_{ads} \tag{17}$$

$$Fe_2O_3\left(h_{vb}^{+}\right) + H_2O_{ads} \rightarrow Fe_2O_3 + HO\bullet_{ads} + H^{+} \tag{18}$$

$$HO\bullet + Substrate_{ads} \rightarrow Substrate_{oxid} \tag{19}$$

$$Fe_2O_3\left(e_{cb}^{-}\right) + Substrate_{ads} \rightarrow Fe_2O_3 + Substrate_{ads}^{-} \tag{20}$$

To confirm this hypothesis, aliquots of the photocatalytic reaction were taken to ESI-MS (Fig. 14). Thiazine-type dyes such as MB can be degraded via hydroxylation, alkylation, deamination, cleavage of S bonds, and the breakage of the ring
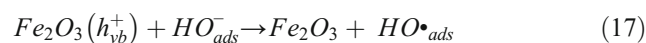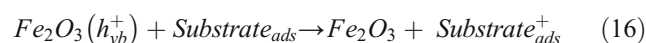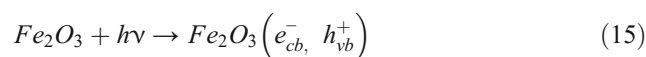
Fig. 13 Kinetics of photocatalytic degradation of MB (a) and RhB (c) dyes in the presence of radicalar (DMSO) and photogenerated hole (EDTA) scavengers. Linear fitting of pseudo-second-order kinetics for MB (b) and RhB (d), respectively

Table 4 Pseudo-second-order kinetic fitting for photocatalytic degradation of MB and RhB dyes in the presence of EDTA and DMSO as scavengers

Parameter	Dye					
	MB			RhB		
	Control	EDTA	DMSO	Control	EDTA	DMSO
R^2	0.9999	0.9988	0.9965	0.9987	0.9918	0.9971
Q_0	2268.4310	1626.0163	2006.6890	7.1787	5.4377	5.9808
K_2	9.73 (10^{-7})	4.21 (10^{-7})	8.87 (10^{-7})	0.1248	0.0282	0.0345

The control experiment was performed without the scavengers

structure. At 0 min, just the parent MB peak with $m/z = 284$ was detected, but after 60 min of UV irradiation, other peaks with different m/z were detected. The peak with $m/z = 301$ indicates hydroxylation of the aromatic ring as previously reported by de Souza et al. (2009) and Pinto et al. (2012), which is only possible if hydroxyl radicals are present in the reaction media. This result suggests the formation of $^\bullet$OH species when the catalyst is irradiated. Also, a peak with $m/z = 240$ appears suggesting the loss of one amine group, which indicates that an oxidation reaction might be taking place in the photogenerated h_{vb}^+ (Oliveira et al. 2007; Castro et al. 2009; Gonçalves et al. 2013).

RhB dye has a parent peak with $m/z = 443$, and after 60 min, a peak with $m/z = 459$ is detected, again showing the generation of $^\bullet$OH species (Fig. 14). However, intermediates from the dealkylation reactions were not observed as seen with MB dye. Photogenerated h_{vb}^+ only migrate to the catalyst surface and cannot go further, differently from $^\bullet$OH species that originated from other catalyst surfaces. Hence, if the dye is rapidly adsorbed on the catalyst surface, a reaction regarding h_{vb}^+ will be favored. Nevertheless, if the adsorption rate is not too fast, the generation of $^\bullet$OH species will govern the dye degradation process instead of h_{vb}^+ species which also

concluded that the dye adsorption mode affects the photocatalytic process kinetics (Kordouli et al. 2015).

The results obtained in this work indicate that the FeDOP material is photocatalytically active with high adsorption capacity. Accordingly, as seen by Mössbauer spectroscopy, its magnetic properties might be tuned in order to improve this special characteristic. The enhancement of the magnetic property will allow an easy recovery after each catalytic process, enabling more efficient catalytic recycling.

Conclusion

The different synthesis conditions resulted in two distinct materials. The first, FeIMP, is a hematite at amorphous silica with a specific surface area of 27 $m^2\ g^{-1}$. The second material, maghemite dispersed over a silica matrix, FeDOP, presented a specific area of 235 $m^2\ g^{-1}$.

Both materials follow a pseudo-second-order kinetic model in the adsorption and photocatalysis of methylene blue and Rhodamine B dyes, wherein the FeDOP has a rate-limiting step governed by the interparticle diffusion process. The

Fig. 14 ESI-MS spectra of the photocatalytic reaction using FeDOP as catalyst MB (**a**) and RhB (**b**)
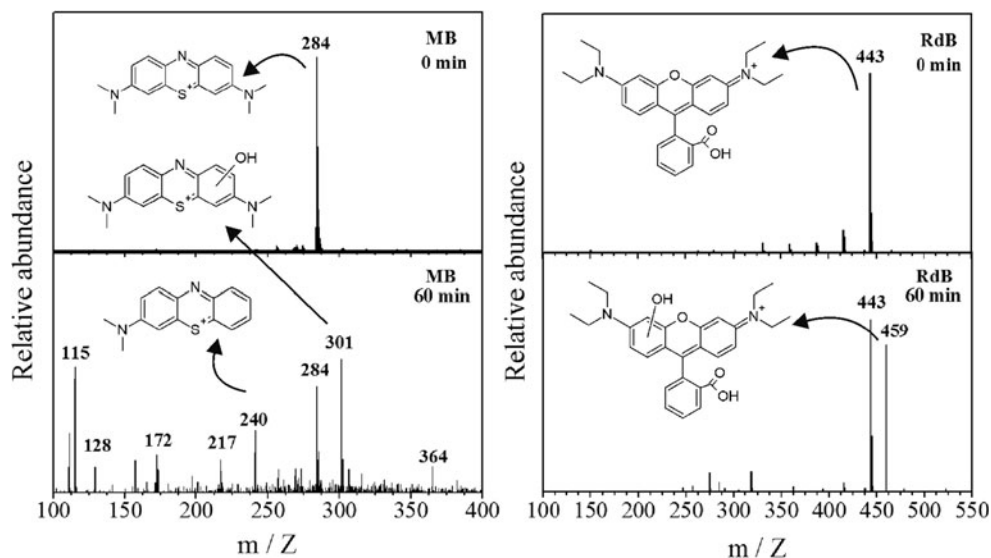
Langmuir adsorption model is that which best describes the adsorption result for both materials and dyes.

Only FeDOP showed photocatalytic activity for dye removal. However, the sorption process should be evaluated beforehand to avoid catalyst poisoning by adsorption. The photogenerated species responsible for the dye degradation might change depending on how the adsorption phenomena take place.

In this study, the dye removal was a combination of both strong adsorption and photodegradation. The pseudo-second-order kinetic model usually exhibits a strong adsorption step, which makes the most active photogenerated species being the photogenerated holes. The $^{\bullet}OH$ species play the major role if the dye adsorption is not vigorous.

References

Ajmal A, Majeed I, Malik N (2014) Principles and mechanisms of photocatalytic dye degradation on TiO_2 based photocatalysts: a comparative overview. R Soc Chem Adv 4:37003–37026. doi:10.1039/c4ra06658h

Al-anber ZA, Al-anber MAS (2008) Thermodynamics and kinetic studies of iron (III) adsorption by olive cake in a batch system. J Mex Chem Soc 52:108–115

Alihosseini A, Taghikhani V, Safekordi AA, Bastani D (2010) Equilibrium sorption of crude oil by expanded perlite using different adsorption isotherms at 298. 15 k. Int J Environ Sci Technol 7:591–598

Bjørgen M, Joensen F, Spangsberg M, et al (2008) Applied Catalysis A : General Methanol to gasoline over zeolite H-ZSM-5 : Improved catalyst performance by treatment with NaOH. 345:43–50. doi:10.1016/j.apcata.2008.04.020

Castro CS, Guerreiro MC, Gonçalves M et al (2009) Activated carbon/iron oxide composites for the removal of atrazine from aqueous medium. J Hazard Mater 164:609–614. doi:10.1016/j.jhazmat.2008.08.066

Cortes J, Araya P (1986) The Dubinin-Radushkevich-Kaganer equation. J Chem Soc Faraday Trans 82:2473–2479

de Souza WF, Guimarães IR, Guerreiro MC, Oliveira LCA (2009) Catalytic oxidation of sulfur and nitrogen compounds from diesel fuel. Appl Catal A Gen 360:205–209. doi:10.1016/j.apcata.2009.03.023

Foo KY, Hameed BH (2010) Insights into the modeling of adsorption isotherm systems. Chem Eng J 156:2–10. doi:10.1016/j.cej.2009.09.013

Gonçalves M, Guerreiro MC, de Oliveira LCA, de Castro CS (2013) A friendly environmental material: iron oxide dispersed over activated carbon from coffee husk for organic pollutants removal. J Environ Manage 127:206–11. doi:10.1016/j.jenvman.2013.05.017

Gong J-L, Wang B, Zeng G-M et al (2009) Removal of cationic dyes from aqueous solution using magnetic multi-wall carbon nanotube nanocomposite as adsorbent. J Hazard Mater 164:1517–22. doi:10.1016/j.jhazmat.2008.09.072

Hasanbeigi A, Price L (2015) A technical review of emerging technologies for energy and water efficiency and pollution reduction in the textile industry. J Clean Prod 95:30–44. doi:10.1016/j.jclepro.2015.02.079

Kordouli E, Bourikas K, Lycourghiotis A, Kordulis C (2015) The mechanism of azo-dyes adsorption on the titanium dioxide surface and their photocatalytic degradation over samples with various anatase/rutile ratios. Catal Today 252:128–135. doi:10.1016/j.cattod.2014.09.010

Litter M (1999) Heterogeneous photocatalysis transition metal ions in photocatalytic systems. Appl Catal B Environ 23:89–114. doi:10.1016/S0926-3373(99)00069-7

Marcelino RBP, Queiroz MTA, Amorim CC, et al (2014) Solar energy for wastewater treatment: review of international technologies and their applicability in Brazil. Environ Sci Pollut Res 762–773. doi: 10.1007/s11356-014-3033-2

Ohtani B (2010) Photocatalysis A to Z—what we know and what we do not know in a scientific sense. J Photochem Photobiol C Photochem Rev 11:157–178. doi:10.1016/j.jphotochemrev.2011.02.001

Oliveira LCA, Gonçalves M, Guerreiro MC et al (2007) A new catalyst material based on niobia/iron oxide composite on the oxidation of organic contaminants in water via heterogeneous Fenton mechanisms. Appl Catal A Gen 316:117–124. doi:10.1016/j.apcata.2006.09.027

Pinto ISX, Pacheco PHVV, Coelho JV et al (2012) Nanostructured δ-FeOOH: an efficient Fenton-like catalyst for the oxidation of organics in water. Appl Catal B Environ 119–120:175–182. doi:10.1016/j.apcatb.2012.02.026

Schwertmann U, Cornell RM (1991) Iron oxides in the laboratory. VCH, Nova York

Schwertmann U, Cornell RM (2003) The iron oxides: structure, properties, reactions, occurences and uses, second edition. Wiley-VCH, Weinheim

Silva AC, Oliveira DQL, Oliveira LCA et al (2009) Nb-containing hematites $Fe_{2-x}Nb_xO_3$: the role of Nb^{5+} on the reactivity in presence of the H_2O_2 or ultraviolet light. Appl Catal A Gen 357:79–84. doi:10.1016/j.apcata.2009.01.014

Srivastava SK, Tyagi R, Pant N (1989) Adsorption of heavy metal ions on carbonaceous material developed from the waste slurry generated in local fertilizer plants. Water Res 23:1161–1165

Sun Q, Yang L (2003) The adsorption of basic dyes from aqueous solution on modified peat-resin particle. Water Res 37:1535–44. doi:10.1016/S0043-1354(02)00520-1

United Nations Department of Economic and Social Affairs (2015) World Population Prospects: The 2015 Revision (ESA/P/WP.241). 1–59. doi: Working Paper No. ESA/P/WP.241

Weber WJ, Morris JC (1963) Kinetics of adsorption on carbon from solution. J Sanit Eng Div 89:31–59

Wu F-C, Tseng R-L, Juang R-S (2009) Initial behavior of intraparticle diffusion model used in the description of adsorption kinetics. Chem Eng J 153:1–8. doi:10.1016/j.cej.2009.04.042

Wu W, Jiang C, Roy VAL (2015) Recent progress in magnetic iron oxide semiconductor composite nanomaterials as promising photocatalysts. Nanoscale 7:38–58. doi:10.1039/C4NR04244A